EFFECT OF RIB SHAPE AND SPLICE LENGTH ON THE STRENGTH OF LAP SPLICES WITHOUT STIRRUPS

T. Ichinose and W. Lin
Department of Architecture, Nagoya Institute of Technology, Japan
J. Bolander, Jr.
Department of Civil and Environmental Engineering, University of California, Davis, USA

Abstract
A numerical model is used to analyze the relationship between radial stress and radial opening at the surface of spliced reinforcing bars. Considering the mechanisms of concrete fracture in front of ribs and the friction at the interface between the concrete and rib face, the local bond-slip relationship is derived and integrated to obtain splice strength. The results indicate that rib shape greatly affects the strength of splices without stirrups when splice length is short.
Key words: Bond strength, rib shape, splice length, slip

1 Introduction

Bond of deformed bars depends mainly on mechanical interaction between the ribs of the bars and the surrounding concrete. Numerous experiments have been performed to investigate the effect of rib shape and splice length on splice strength in reinforced concrete beams without stirrups. Those experiments have indicated that when stirrups are not used, 1) larger splice length reduces average bond strength; and 2) the effects of bar deformation details are less significant. However, this information is empirical and, by

itself, is not adequate for developing comprehensive lap splice models.

This paper uses an analytical approach which provides a bird's eye view on the effects of the rib shape and splice length on the strength of splices and reasons for the experimental findings. The analysis consists of three steps: 1) obtain the relationship between radial stress and radial opening at the bar surface using a numerical model; 2) derive the local bond-slip relationship considering the mechanisms of concrete fracture in front of ribs and the friction at the interface between the concrete and rib face; and 3) integrate the local bond-slip relationship to calculate the splice strength considering both the equilibrium between the bar axial stress and bond stress resultants and the compatibility of strains and slip. The slip distribution changes abruptly at the discrete locations along the splice where flexural cracking occurs.

2 Radial stress versus radial opening at the bar surface

2.1 Rigid-body-spring network model of beam cross-section

The beam cross-section of Fujii et al. (1993) is partitioned into an assemblage of rigid bodies, or cells, interconnected along their boundaries through flexible interfaces (Fig. 1a and 2). This type of rigid-body-spring network was first introduced by Kawai (1978). Each rigid cell has two translatory and one rotational degrees of freedom defined at some point within its interior. Normal, tangential, and rotational springs act at the midpoint of each boundary segment; spring stiffnesses are set to approximate the elastic properties of the continuum (Kawai, 1978).

To reduce mesh bias on potential crack directions, and to automate the meshing process, the network geometry is defined by a Voronoi diagram
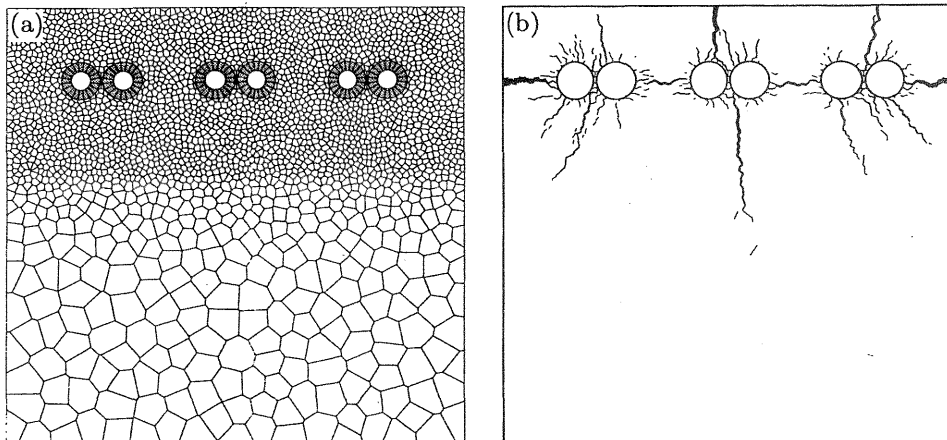
(a) domain discretization   (b) crack patterns just after peak load

Fig. 1 Rigid-body-spring network modeling of beam cross-section

based on randomly distributed nuclei. The aforementioned computational degrees of freedom are assigned at the Voronoi cell nuclei. Material nonlinearity is simulated by progressively degrading the elastic properties of the intercell springs. Notably, tensile softening of the normal spring is controlled so as to consume proper fracture energy, as shown by the stress-strain diagram in Fig. 3 where f_t is tensile strength, G_f is fracture energy, and h is the distance (normal to the boundary segment) between contiguous nuclei. Bazant et al. (1990) used this approach for softening trusses within a rigid particle modeling of cement composites.

Pressure loading is applied within stiff elastic rings (Fig. 1c), which push radially against the concrete to simulate the opening actions of deformed bars. Tangential stiffness at the bar-concrete interface is released. Young's Modulus and the tensile strength of the concrete are 2.5E+04 MPa and 2.9 MPa, respectively. The latter value is based on $0.33\sqrt{f_c}$, where f'_c (=75.7MPa) is reported compressive. In the absence of experimental measurements, fracture energy was assumed to be 0.05 N/mm, which is less than the normal range used for macroscopic fracture analyses.

2.2 Numerical results

For each pressure level, the average opening of each ring is computed. Knowing the stiffness of the rings, the corresponding average radial pressures on the concrete can be determined. Fig. 4 gives the numerical results for average radial pressure versus average radial opening determined from all six bars. Fig. 1b shows the cracking pattern in the model just beyond peak load, as indicated by point A on the pressure-opening curve. The peak load is somewhat large due, in part, to unnatural restraint at the bar-concrete interface. Changing fracture energy does not appreciably affect peak load, but significantly affects post-peak behavior.
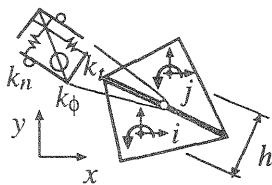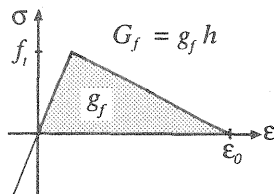

Fig. 2 Two-cell assembly

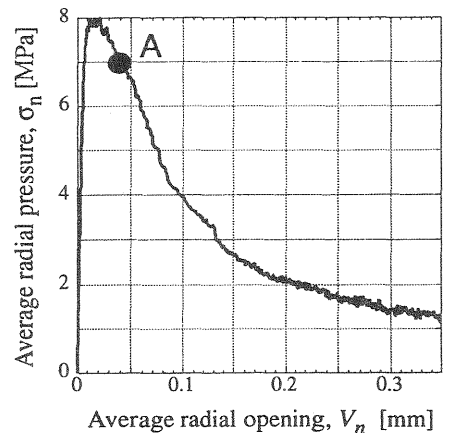Fig. 3 Stress-strain curve for concrete in uniaxial tension

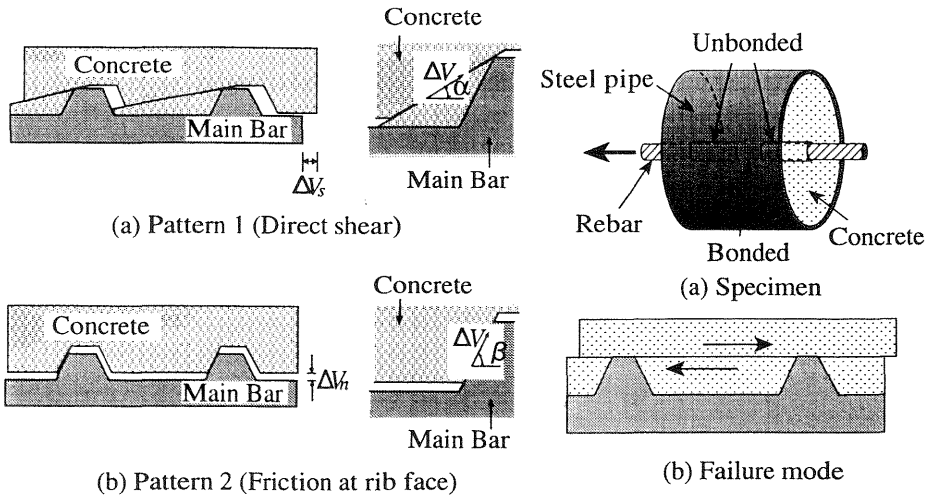Fig. 4 Average radial pressure versus average radial opening

1303

(a) Pattern 1 (Direct shear)

(a) Specimen

(b) Pattern 2 (Friction at rib face)

(b) Failure mode

Fig. 5. Failure patterns in front of ribs   Fig. 6. Pullout test with steel pipe

3 Local bond-slip relationship

3.1 Assumptions

We assume that one of the following two patterns of failure causes incremental slip ΔV_s.

Pattern 1: Direct shear of concrete, as shown in Fig. 5 (a). The angle of the fracture plane, α, is determined so that the local bond stress τ (shown in Fig. 7) is minimized. This failure occurs when the shear stress at the potential failure plane reaches τ_{max}, which is given as a function of concrete strength:

$$\tau_{max} = 1.7 f_c^{'0.85} \text{ [MPa]} \tag{1}$$

This equation is based on the pullout tests of Akashi et al. (1991) shown in Fig. 6 (a) , where the steel pipe is thick enough to be considered as rigid and the bar is pulled out in direct shear mode as shown in Fig. 6 (b).

Pattern 2: Friction at rib face, as shown in Fig. 5 (b). β is the angle of rib face; the friction coefficient μ is assumed to be 0.5.

The failure pattern is decided so that the local bond stress τ is minimized. The failure pattern may change as the slip increases.

3.2 Compatibility and equilibrium local to bar rib

To evaluate local bond stress τ, force equilibrium at a rib is considered as shown in Fig. 7 and

$$R_s \tau = S(q_n \sin\alpha + q_t \cos\alpha) \tag{2}$$

$$R_s \sigma_n = S(q_n \cos\alpha - q_t \sin\alpha) \tag{3}$$

where q_n and q_t are the stresses normal and tangential to the failure plane, respectively; R_s is the length interval between the ribs; S is the length of the failure plane, which is normally $S = H_d / \sin\alpha$, and σ_n is the radial pressure
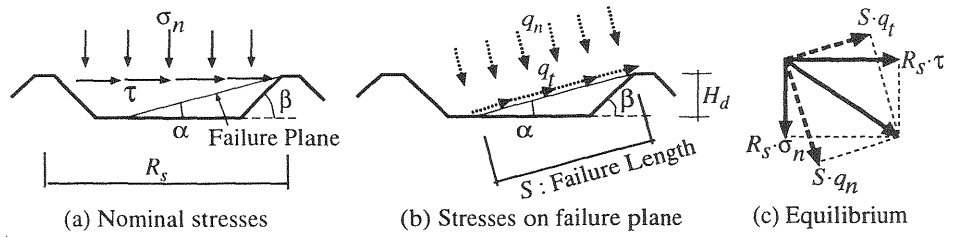
(a) Nominal stresses   (b) Stresses on failure plane   (c) Equilibrium

Fig. 7. Stress on potential failure plane in front of a rib

given by the preceding analysis. For pattern 2, α should read β.

The tangential stress q_t is given by one of the following equations depending on the failure patterns in Fig. 5;

$$q_t = \tau_{max} \qquad \text{(4) (Direct shear)}$$

$$q_t = \mu q_n \qquad \text{(5) (Friction at rib face; } m = 0.5 \text{)}$$

Eliminating q_n and q_t from Eq. 2 using Eqs. 3 through 5, we obtain τ as a function of α, which is determined so that τ be minimized. Thus, τ is a function of σ_n. Furthermore, σ_n is a function of V_n, whose increment is determined from ΔV_s as follows.

$$\Delta V_n = \Delta V_s \tan \alpha \qquad \text{(6) (Direct shear)}$$

$$\Delta V_n = \Delta V_s \tan \beta \qquad \text{(7) (Friction at rib face; } m = 0.5 \text{)}$$

Thus, we can obtain the local bond-slip (τ-V_s) relationship since τ is a function of V_s, as just described.

3.3 Effect of rib shape on local bond-slip relationship

The beam specimens of Fujii et al. (1993) without stirrups are Analyzed. The details of rib shape and the calculated relationship between the bond stress τ and the slip V_s are shown in Fig. 8. The local bond stress-slip relationships are different because of the differences in rib shape. The Fujii speci-
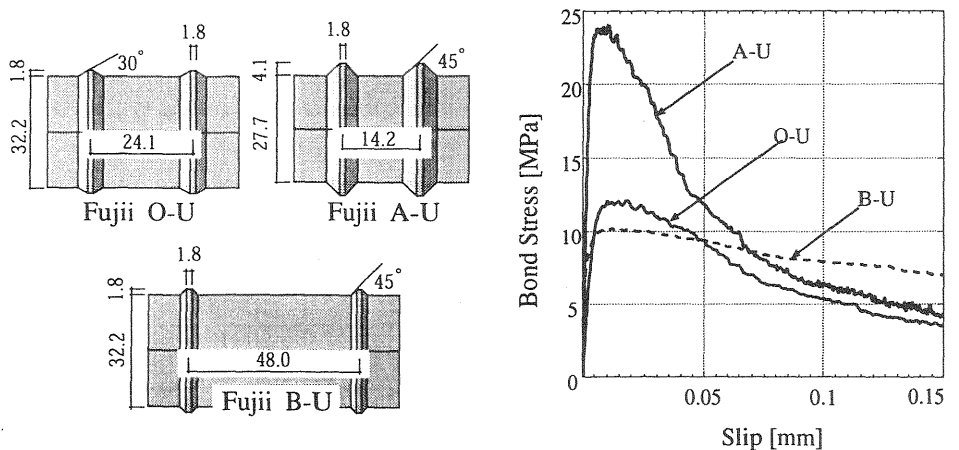

Fig. 8. Rib shape and local bond-slip relationship

mens O-U, A-U and B-U have different rib heights and rib spacings (O-U: ordinary rib shape; A-U: high rib with narrow spacing; B-U: low rib with wide spacing). The calculated local bond strength of the specimen A-U, which has a higher rib height to spacing ratio (H_d/R_s=28.6%) is much larger than those of the specimens O-U and B-U with lower rib height to spacing ratios (H_d/R_s =7.4% and 3.7%). The softening of A-U is also larger than the other two, which affects the splice strength as will appear later. The failure pattern of specimens A-U and O-U corresponded to friction at rib face at every slip level; the larger rib face angle of A-U resulted in larger strength and rapid softening. The failure pattern of the specimen B-U was predominantly direct shear with a failure plane angle of about 30 deg. because of the small H_d/R_s ratio. This resulted in the ductile behavior after the peak strength.

4 Distribution of stress, strain and slip

4.1 Assumptions
The following assumptions are used for analysis.
(a) There are three flexural cracks as shown in Fig. 9. One crack is at the center of splice and the other two are at the ends of splice.
(b) Concrete strain between flexural cracks is negligibly small.
    We should note that the bond-slip relationship derived in the preceding section is based on the assumption that the radial displacement at each spliced bar increases at the same rate. Thus, we implicitly assumed that the slips of the spliced bars also increase at the same rate. Due to the preceding assumption (a), however, the slip of the bar extending from the left, V_{sL}, may differ from that of the right bar, V_{sR}. Thus, we add the following assumptions.
(c) The average of the bond stresses of the spliced bars, τ_L and τ_R, is a function of the average of the slip of the bars as follows, where τ indicates the bond-slip functional relation given in the previous section.

$$\frac{|\tau_L|+|\tau_R|}{2} = \tau\left(\frac{|V_{SL}|+|V_{SR}|}{2}\right) \tag{8}$$

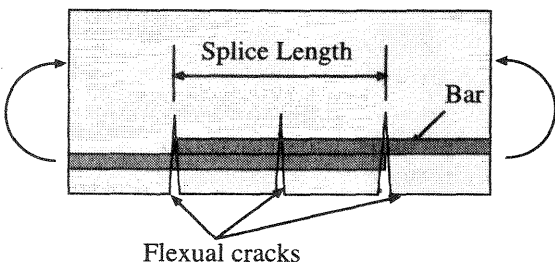(d) The ratio of the bond stresses of the spliced bars is proportional to the
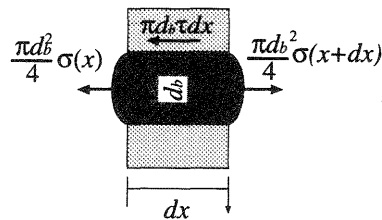

Fig. 9. Assumed flexural cracks

Fig. 10. Equilibrium of bar stress within elemental length

ratio of the slips so that the bar with larger slip has larger bond stress.

$$\frac{\tau_L}{\tau_R} = \frac{V_{SL}}{V_{SR}} \tag{9}$$

4.2 The definition of slip and the basic equation

The displacements of the bar and the concrete in the longitudinal direction are defined as v_s and v_c respectively. We define the slip of the bar V_s as follows.

$$V_s = v_s - v_c \tag{10}$$

Differentiating Eq.(10) with respect to x, the distance from the center of the splice and assuming that the concrete strain is negligibly small

$$\frac{dV_s}{dx} = \varepsilon_s \tag{11}$$

where ε_s is the axial strain of the bar. Equilibrium between bar axial stress and bond stress shown in Fig. 10 for an elemental length dx of the bar gives

$$\frac{\pi d_b^2}{4}[\sigma(x+dx) - \sigma(x)] = \pi \cdot d_b \cdot \tau \cdot dx \tag{12}$$

where d_b is the bar diameter. If the spliced bar remains elastic and E is elastic modulus of steel, then

$$\frac{d\varepsilon_s}{dx} = \frac{4}{Ed_b}\tau \tag{13}$$

Differentiating Eq.(11) and substituting the result into Eq.(13) we obtain the basic equation for analysis, that is

$$\frac{d^2 V_s}{dx^2} = \frac{4}{Ed_b}\tau \tag{14}$$

Integrating this equation numerically, we have the distribution of slip and bond stress along the splice length.

4.3 Effect of rib shape on splice strength

The specimens of Fujii et al. (1993) are analyzed. The rib details of the specimens, the calculated results and experimental results for bond strength are shown in Table 1.

From Table 1 we can see the analytical results overestimate the experimental results. However, the analytical strength of A-U is about 1.2 times of those of O-U and B-U as was in the experiments. Note that the local bond strength of A-U is about 2 times of the other two (Fig. 8).

The calculated slip distributions of the bars extending to the right are shown in Fig. 11. The slip of the bars extending to the left has an inverse pattern around center of the splice with an opposite sign. The discontinuity of the slip at $x = 228$ indicates the crack width at the center of the splice. The slip at the right end plus some pullout from the right concrete (not calcu-

Table 1. Specimens data and analytical results

Specimen	A_L	d_b	τ_A	τ_E	τ_A / τ_E
Fujii O-U	457	35.8	7.77	5.00	1.55
Fujii A-U	457	35.8	9.87	5.95	1.66
Fujii B-U	457	35.8	8.10	5.00	1.62

Where A_L: splice length (mm)
         τ_A: analytical average bond strength (MPa)
   and τ_E: experimental average bond strength (MPa)

lated in the analysis) gives the crack width at the ends of the splice. The crack width at the center is smaller than those at the ends, as was observed in the experiment.

The calculated bond stress distributions are shown in Fig. 12. While the bond stress distributions are different, the average bond strengths are similar as shown in Table 1. In other words, the high peak strength of A-U does not significantly affect the average bond strength.

The calculated bar strain distributions are shown in Fig. 13. The strains increase monotonically in the left side of the splice, whereas in the right side, the strains once decrease due to the negative bond stresses shown in Fig. 12, and then increase until reaching about twice the strains at the center.

4.4 Effect of splice length on splice strength

To provide a bird's eye view on the effect of the splice length, we simulate specimens with the same rib shapes as Fujii's but different splice lengths (ranging from 6.4 to 25.5 times the bar diameter). The calculated results are shown in Fig. 14. The results provided by the equations of Orangun et al. (1977) and Darwin et al. (1996) are also given, where the effect of the rib
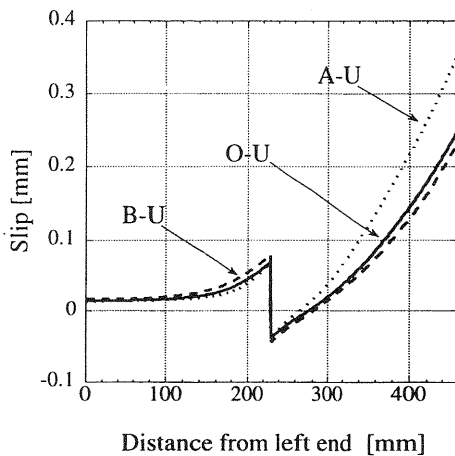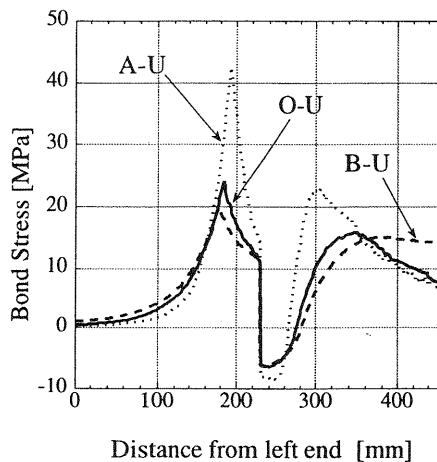
Fig. 11. Slip distribution

Fig. 12. Bond stress distribution

shape is ignored. The experimental results are indicated by the solid circles. The analytical results of the O-U series shows a tendency similar to Orangun's and Darwin's. On the other hand, the effect of splice length is larger in the case of the A-U series and is smaller in the case of the B-U series. Noting that the splice length is normally larger than 20 times of bar diameter, we may conclude that the effect of rib shape on average bond strength is small in normal situations.

The calculated bond stress distributions of the simulated specimens with the splice length of 6.4 times of bar diameter are shown in Fig. 15. This explains the higher average bond strength of the A-U specimen with very short splice length.
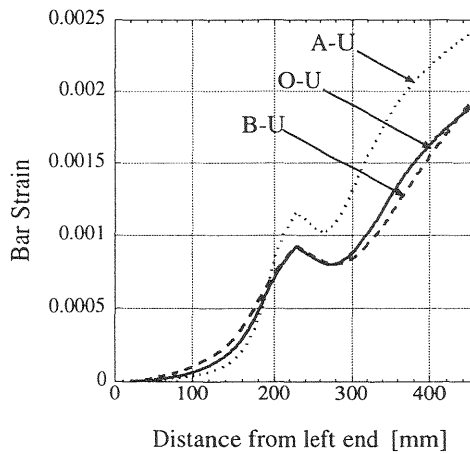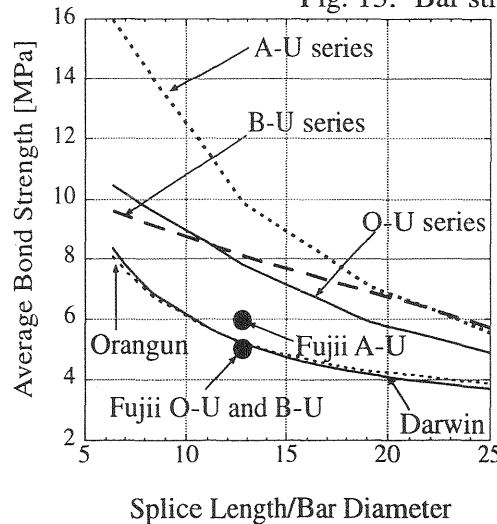
Fig. 13. Bar strain distribution

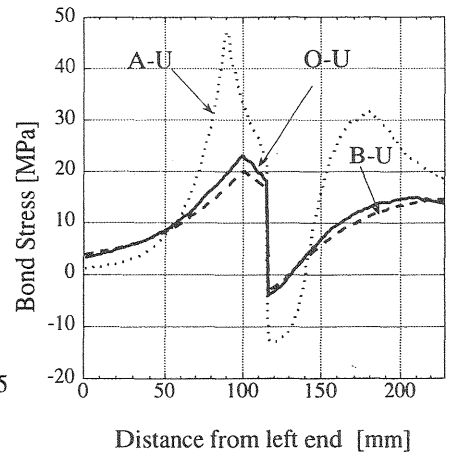Fig. 14. The effect of splice length on bond strength

Fig. 15. Distribution of bond stress of simulated specimens

5 Conclusions

The effects of rib shape and splice length observed through the analysis agreed with those obtained by the experiments and the empirical equations, though the analysis overestimated the splice strengths. If the assumptions of this study are correct, the following conclusions are obtained.

(1) Rib shape greatly affects the local bond-slip relationship. Splice with higher ratio of rib height and rib spacing (H_d/R_s) has larger local bond strength but softens more rapidly after peak.

(2) The effects of rib shape on splice strength may be remarkable when splice length is very short, but the effect may be small when splice length is large.

(3) The effects of splice length on splice strength are significant when the ratio of rib height and rib spacing (H_d/R_s) is large. For the analyses given here, doubling the splice length with ordinary rib shape from $10.d_b$ to $20.d_b$ resulted in a 30% decrease in average bond strength, whereas in the case of higher ribs the decrease was 45%.

6 References

Akashi, J., Fujii, S., and Morita, S. (1991) Effects of concrete strength and deformation shape on bond strength. **Proceedings of The Japan Concrete Institute**, 18 (2), 127-132.

Bazant, Z.P., Tabbara, M.R., Kazemi, M.T. and Pijaudier-Cabot, G. (1990) Random particle model for fracture of aggregate or fiber composites. **ASCE J. Engng. Mechanics,** 116, 1686-1705.

Darwin, D., Zuo, J., Tholen, M. L. and Idun, E. K. (1996) Development length criteria for conventional and high relative rib area reinforcing bars. **ACI Structural Journal**, 93 (3), 347-359.

Fujii, S, Kimura, H and Jirsa, J. O. (1993) Effect of bar surface deformation on splitting bond failure of lap splice. **AIJ Summaries of Technical Papers of Annual Meeting**, 227-228. (in Japanese)

Kawai, T. (1978) New discrete models and their application to seismic response analysis of structures. **Nuclear Engng. Design,** 48, 207-229.

Orangun, C. O. , Jirsa, J. O. and Breen, J. E. (1977) A reevaluation of test data on development length and splices. **ACI Journal,** 74 (3), 114-122.